

Anneke Meyer<sup>1</sup>, Marko Rak<sup>1</sup>, Daniel Schindele<sup>2</sup>, Simon Blaschke<sup>2</sup> Martin Schostak<sup>2</sup>,  
Andriy Fedorov<sup>3</sup>, Christian Hansen<sup>1</sup>

# Towards Patient-Individual PI-RADS v2 Sector Map: CNN for Automatic Segmentation of Prostatic Zones from T2-Weighted MRI

Pre-print Version

<sup>1</sup> Faculty of Computer Science & Research Campus STIMULATE,  
University of Magdeburg, Germany

<sup>2</sup> Clinic of Urology and Pediatric Urology, University Hospital Magdeburg, Germany

<sup>3</sup> Department of Radiology, Brigham and Women's Hospital, Harvard Medical School, Boston, USA

# TOWARDS PATIENT-INDIVIDUAL PI-RADS V2 SECTOR MAP: CNN FOR AUTOMATIC SEGMENTATION OF PROSTATIC ZONES FROM T2-WEIGHTED MRI

Anneke Meyer<sup>1</sup>, Marko Rak<sup>1</sup>, Daniel Schindele<sup>2</sup>, Simon Blaschke<sup>2</sup>,  
Martin Schostak<sup>2</sup>, Andriy Fedorov<sup>3</sup>, Christian Hansen<sup>1</sup>

<sup>1</sup> Faculty of Computer Science & Research Campus STIMULATE, University of Magdeburg, Germany

<sup>2</sup> Clinic of Urology and Pediatric Urology, University Hospital Magdeburg, Germany

<sup>3</sup> Department of Radiology, Brigham and Women's Hospital, Harvard Medical School, Boston, USA

## ABSTRACT

Automatic segmentation of the prostate, its inner and surrounding structures is highly desired for various applications. Several works have been presented for segmentation of anatomical zones of the prostate that are limited to the transition and peripheral zone. Following the spatial division according to the PI-RADS v2 sector map, we present a multi-class segmentation method that additionally targets the anterior fibromuscular stroma and distal prostatic urethra to improve computer-aided detection methods and enable a more precise therapy planning. We propose a multi-class segmentation with an anisotropic convolutional neural network that generates a topologically correct division of the prostate into these four structures. We evaluated our method on a dataset of T2-weighted axial MRI scans (n=98 subjects) and obtained results in the range of inter-rater variability for the majority of the zones.

*Preprint version of the author. This work has been submitted to the IEEE for possible publication. Copyright may be transferred without notice, after which this version may no longer be accessible.*

**Index Terms**— MRI, prostate zone segmentation, PI-RADS v2 sector map, deep convolutional neural networks, therapy planning, computer-aided diagnosis

## 1. INTRODUCTION

Multiparametric MRI is gaining increasing importance in supporting the diagnosis, localization and therapy planning of prostate cancer (PCa). For the purpose of standardizing this process, Prostate Imaging - Reporting and Data System version 2 (PI-RADS v2) [1] was developed to give guidelines for MRI protocols, interpretation and lesion detection. PI-RADS v2 interpretation takes into account the anatomical zones of the prostate introduced by McNeal [2] who partitioned the prostate into four anatomical zones: peripheral zone (PZ), anterior fibromuscular stroma (AFS), transition zone (TZ) and central zone (CZ). Depending on whether the lesion is located in TZ or PZ, different MRI modalities are majorly used for assigning a PI-RADS score.

In this work we investigate a method based on convolutional neural networks (CNNs) for the automatic and simultaneous segmentation of PZ, TZ, AFS and distal prostatic urethra (DPU) from T2-weighted (T2w) MR images (see Fig. 1). The choice for these zones is based on the PI-RADS v2 sector map that should allow for better communication of lesion locations by employing various sectors for the prostate, urethral sphincter and seminal vesicles. A reliable automatic segmentation of the structures can improve the consistency of lesion location assignment and reduce cognitive workload for

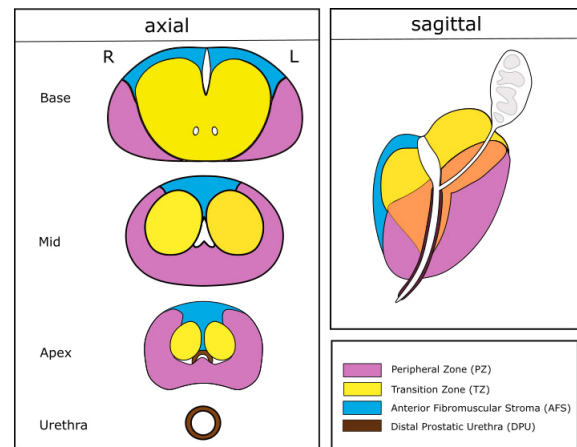


**Fig. 1.** Anatomical division of the prostate into PZ, TZ, AFS and DPU. Illustration recreated according to [1].

clinicians [3]. Moreover, automatic segmentation of PZ and TZ will enable better repeatability for longitudinal studies [4] and will provide valuable information for computer-aided diagnosis systems, specifically for clinical significance classification of lesions [5]. Next to PZ and TZ, AFS and DPU are relevant for planning of PCa treatment, for example resection, radiation dose and focal therapy. As these four structures are all located to some extent in the prostate gland, we propose to segment them simultaneously in a multi-label fashion. CZ is not considered in this work as it is not distinguishable in most cases and has furthermore no effect on the PI-RADS v2 score. Here, we consider TZ as combination of TZ and CZ, also known as central gland.

Various segmentation algorithms for the whole prostate have been presented in the past, varying from deformable models to atlas-based segmentation, machine learning approaches and hybrids of these methods. An overview on these algorithms can be found in [6]. As the prostate has high variability in shape and appearance, convolutional neural networks (CNNs) that can better cope with these problems, gained popularity for segmentation. Variants of the 2D U-Net that was developed by Ronneberger et al. [7] are frequently used as in [8, 9].

Similarly, zonal segmentation of the prostate has been performed with deformable models, atlas-based segmentation and machine learning. Several of these approaches use multiparametric MRI [10, 11, 12]. The first work that inputs only T2w MRI was proposed

by Toth et al. [13] who used multiple coupled levelsets for incorporating shape and appearance information into the algorithm. Qiu et al. [14] take into account spatial region consistency of the zones and case-dependent appearance after the user initialized the method with prostate boundary points. Chilali et al. [15] performed segmentation by use of atlas images and evidential C-Means clustering.

So far, there exist only two approaches that integrate CNNs into the segmentation of zonal anatomy: Clark et al. [12] proposed an architecture with four consecutive 2D CNNs. The networks are responsible for detection and consecutive segmentation of the prostate in a first and second step which is followed by detection and segmentation of the TZ in a third and fourth step. The second work by Mooj et al. [16] segments the TZ and PZ by means of a U-Net based architecture that takes into account the anisotropic resolution of MRI scans: instead of overall 3D convolutions and 3D MaxPoolings, the authors employ 2D convolutions and 2D MaxPooling in the high resolution directions and only use 3D architecture in the last resolution layer.

In the following section, we propose a 3D U-Net variant that also takes only the highly anisotropic axial T2w images into account and generates a gap-free segmentation of prostatic zones for therapy planning and computer aided diagnosis. Including only T2w images has the advantage that we need less resources and that we do not have to coregister other sequences. Previous works on automatic zonal segmentation have been limited to TZ and PZ. Our segmentation additionally targets DPU and AFS that are important structures for therapy planning. To the best of our knowledge, we are the first to incorporate these structures for automatic segmentation in MRI. We evaluate our network's output with manual segmentations from three different experts and compare the results with inter-rater variability of the three experts. As an additional contribution, we will make our ground truth segmentations public for other researchers by the time of manuscript publication.

## 2. METHOD

Due to the inhomogeneous appearance of the prostate and its inner structures (see Fig. 3), CNNs were our choice of technique for zonal segmentation. We propose to use a variant of the 3D U-Net [17]. In the following we describe the network architecture and its training as well as pre- and postprocessing.

### 2.1. Network Architecture

The U-Net and its three-dimensional variant consist of a contracting encoder part and an expanding decoder part (see Fig. 2). The first part analyses and downsamples the image to increase the receptive field of the network while the expanding path synthesizes the filters back to the input resolution and creates a segmentation. In the encoder part, the image is downsampled by means of three resolution steps. Each layer in one resolution step consists of two  $3 \times 3 \times 3$  convolution filters with ReLU activation and a successive MaxPooling operation. On the way down, the number of filters increases from 16 for the first layer to 256 in the bottom layer. In contrast to the original architecture, we used anisotropic  $2 \times 2 \times 1$  MaxPooling to take the highly anisotropic input data into account. Only the last MaxPooling is isotropic with  $2 \times 2 \times 2$ . Similarly, the decoder path with transposed convolution ( $3 \times 3 \times 3$  kernel) employs a stride of 2 in each dimension for the first layer. It is followed by two  $3 \times 3 \times 3$  convolution layers with decreasing number of filters. With respect to the anisotropic downsampling, we used transposed convolution with a stride of  $2 \times 2 \times 1$  for the last two decoder resolution steps. As in

the original architecture, we employed skip connections to transfer high resolution information from the encoder path to the same level of the synthesis path. Batch normalization after every convolution was added for faster learning. As regularization, dropout with a rate of 0.5 was included in the bottom most layer and in the decoding layers. The last layer of the network is a  $1 \times 1 \times 1$  convolution with softmax activation function and a resulting output of 5 channels: one each for TZ, PZ, DPU, AFS and background. Due to its 'winner-takes-it-all'-nature, the softmax function is optimal for creating a preferably non-overlapping multi-class segmentation.

### 2.2. Dataset and Preprocessing

The dataset used in this work consists of 98 T2w series selected randomly from the publicly available SPIE-AAPM-NCI PROSTATEx challenge dataset [18]. The images were acquired by two different types of Siemens 3T MRI scanners (MAGNETOM Trio and Skyra) with a body coil. The ground truth segmentation of the prostate zones was created on the axial images with 3D Slicer [19] by a medical student and subsequently corrected by an expert urologist. All volumes were resampled to a spacing of  $0.5 \times 0.5 \times 3$  mm which corresponds to the highest in-plane resolution and maintains the relation of in-plane to inter-plane resolution of the dataset. A bounding box ROI of the prostate was automatically extracted with help of sagittal and coronal T2w series: the ROI was defined as the intersecting volume of the three MR sequences. Prior to normalization of image intensity to an interval of [0,1], the intensities were cropped to the first and 99th percentile. For segmentation, only axial images were considered. They were split into training ( $n=78$ ) and test data ( $n=20$ ). The training data was augmented by random application of the following transformations: left-right flipping, 3D rotation, scaling and 3D translation. Instead of nearest neighbor interpolation, we used a shape-based interpolation as proposed in [20] for the augmentation which produced smoothly transformed segments. For evaluating the inter-rater variability and the performance of the automatic segmentation, a second test data ground truth was created by a second expert urologist with the help of another medical student. Additionally, a third expert segmentation was generated by an assistant radiologist (only 10 of the 20 test cases).

### 2.3. Network Training

We trained our network with the negative Dice Similarity Coefficient (DSC) loss function. For our multi-class segmentation, the loss function was:

$$loss = - \sum_{z \in \{TZ, PZ, DPU, AFS\}} \frac{2 \sum_i^N p_{z,i} g_{z,i}}{\sum_i^N p_{z,i}^2 + \sum_i^N g_{z,i}^2}$$

with  $N$  being the total number of voxels and  $p_{z,i}$  the predicted voxels and  $g_{z,i}$  the ground truth binary voxels of zone  $z$ . Adam optimizer [21] with learning rate of  $5e^{-05}$  was employed and the network was trained for a maximum of 1000 epochs with learning rate decay and with a batch size of 2 on a NVIDIA TitanX GPU. The total number of trainable parameters for the proposed model was 6,098,245. In a 4-fold cross validation, the optimal learning rate schedule and number of training epochs was determined for a final training run that included all of the 78 training volumes (approx. 60 hours training time and less than 1 second per image for prediction).

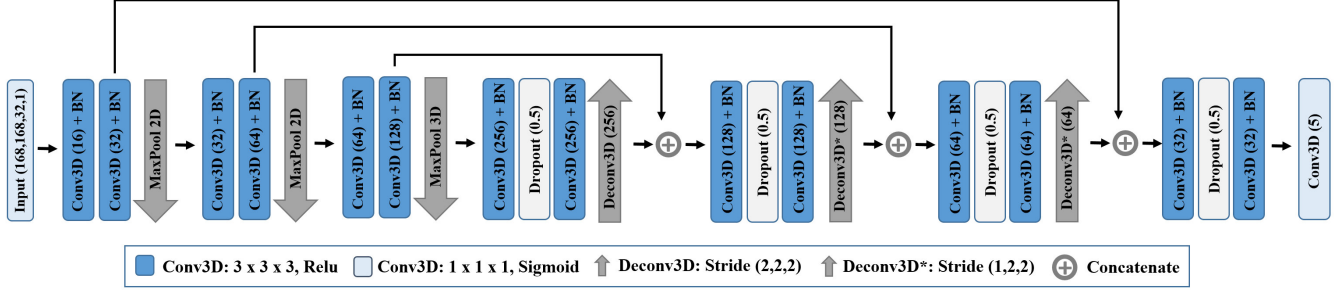


**Fig. 2.** Proposed anisotropic architecture of the network for zonal segmentation. Architecture is based on the 3D U-Net [17].

**Table 1.** Automatic and manual segmentation evaluation. Autom. is the presented network that considers anisotropy of the data. Autom. ISO is the output of the original U-Net architecture that does not consider the anisotropy. Mean absolute symmetric distance (MAD) in *mm*.

Comparison	TZ		PZ		DPU		AFS	
	DSC	MAD	DSC	MAD	DSC	MAD	DSC	MAD
Autom. vs. Expert1	87.6 ± 6.6	0.93 ± 0.32	79.8 ± 5.1	0.84 ± 0.50	75.2 ± 7.2	0.72 ± 0.34	41.1 ± 14.4	3.11 ± 2.06
Autom. ISO vs. Expert1	87.4 ± 6.3	0.97 ± 0.28	78.7 ± 5.0	0.88 ± 0.45	73.9 ± 8.2	0.70 ± 0.31	38.3 ± 15.0	3.22 ± 2.14
Autom. vs. Expert2	86.3 ± 6.9	1.08 ± 0.37	78.2 ± 3.8	1.00 ± 0.63	58.1 ± 8.9	1.51 ± 0.69	38.8 ± 16.5	3.54 ± 2.76
Expert1 vs. Expert2	87.8 ± 5.8	0.86 ± 0.31	81.8 ± 3.4	0.70 ± 0.35	60.6 ± 8.9	1.33 ± 0.49	51.0 ± 11.1	1.91 ± 1.10
Autom. vs. Expert3	81.7 ± 6.5	1.23 ± 0.25	77.5 ± 4.7	0.97 ± 0.60	61.5 ± 6.2	1.37 ± 0.52	33.0 ± 14.1	4.45 ± 2.38
Expert1 vs. Expert3	82.8 ± 5.7	1.07 ± 0.34	78.0 ± 5.4	1.02 ± 0.60	64.1 ± 4.9	1.26 ± 0.39	46.8 ± 15.1	2.42 ± 1.24

#### 2.4. Postprocessing

As the segmentation output from the network may contain isolated regions, we implemented connected components analysis and a distance-based hole filling as postprocessing to guarantee topological correctness. First, for every region a connected components analysis was applied and only the largest component was kept. Voxels resulting in a label-free state after connected components were now assigned a new label with:

$$z \in \{TZ, PZ, DPU, AFS\} \max SDF(z)$$

with  $SDF(z)$  being a signed euclidean distance function that assigns positive values inside and negative values outside the segmentation. Thus, every voxel that had label-free state, gets assigned to the zone of the nearest labeled voxel according to the shape-based distance measure.

### 3. RESULTS AND DISCUSSION

The performance of the presented model trained on 78 images was tested on 20 images which were not considered for training. The evaluation measures are the Dice similarity coefficient (DSC) and mean absolute symmetric distance (MAD), computed as in [22]. Three example results and their corresponding manual segmentations from two experts are given in Fig. 3. The quantitative results evaluated against the different experts can be found in Tab. 1. The first row represents the comparison of the proposed anisotropic automatic segmentation with the expert, who also created the manual segmentations for training. TZ obtains a DSC of 87.6%, PZ achieves a DSC of 79.8% and DPU and AFS result in DSCs of 75.2% and 41.1% respectively. A comparison of these results with those from the isotropic standard network (second row) indicates an improvement of segmentation outcome for PZ, DPU and AFS by employing our anisotropic network. Wilcoxin signed rank p-test resulted in a

p-value of 0.015 for PZ. For the other zones no statistical evidence could be gained due to the small test sample size.

Furthermore, Tab. 1 shows the evaluation metrics obtained by comparing segmentations generated by different experts. Our results for TZ and PZ are in the range of inter-rater variability (compared to the fourth and sixth row). On DPU, our method is even better than the inter-rater difference due to deviation of the experts segmentation in diameter and proximal length. The DSC for the inter-rater comparison of the AFS are 51.0% and 46.7%. Hence, unlike the other zones, the manual segmentations for the AFS are considerably better than the automatic performance.

Smaller volumes generally have the tendency to obtain lower accuracy for region-based measures (e.g. DSC) because smaller errors have a larger weight on the overall measure. Consequently, it is not surprising that DPU and AFS obtained worse results than TZ and PZ. Distance-based measures such as MAD show that the quality of automatic DPU segmentation is still good. On the other hand, regarding the AFS, our method needs improvement. The high standard variance demonstrates that some cases are nearly as good as manual segmentations but many cases are not. The clinicians confirmed that the AFS is the most difficult structure to segment as boundaries are not clearly visible for a large part and the structure has high variety of shape and appearance. Thus, even the inter-rater variability is very high. We also expect the intra-rater variability to be high, but need to confirm this with further experiments in future work.

Another information we can extract from Tab. 1 is the higher accuracy of automatic segmentations compared to the expert who created the training data (Expert1) in contrast to accuracy evaluated against other expert segmentations. This demonstrates the bias that is introduced into the training data by only including segmentations from one clinician. For better performing models, one needs to include more clinicians into the data generation process. We assume that this could improve the segmentation outcome of the AFS, too, as in such a case the manual segmentations may be more consistent.

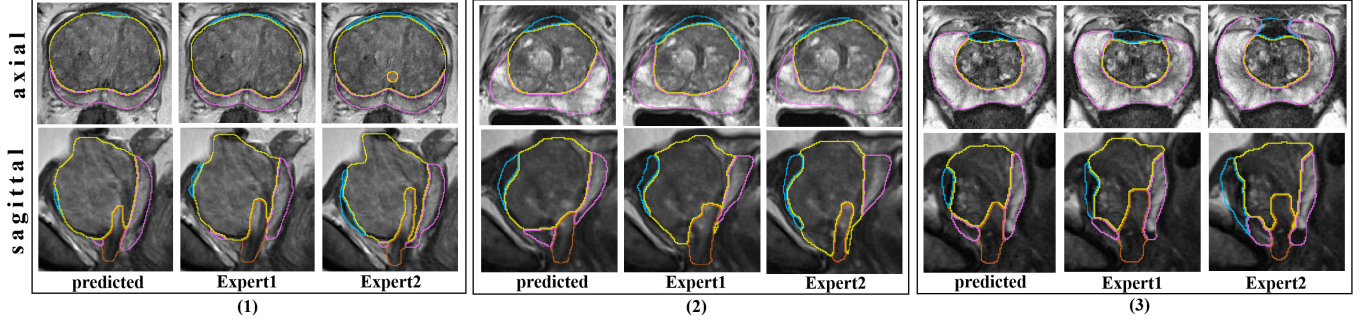


**Fig. 3.** Examples for predicted and manual segmentations of PZ (purple), TZ (green), AFS (blue) and DPU (brown). Worst (1), mean (2) and best (3) automatic segmentation result according to DSC sum over all zones. Segmentations were upsampled for visualization purposes.

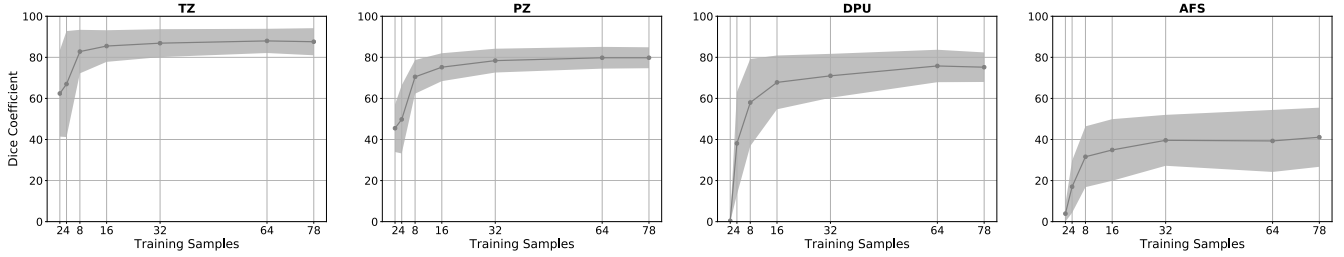


**Fig. 4.** Effect of number of training samples on test accuracy for the four zones: mean and standard deviation ( $\mu$  and  $\pm\sigma$ ) of Dice Coefficient.

Fig. 4 illustrates the effect that the increasing amount of training data has on the performance regarding the DSC. While the experiment suggests that increasing the number of training samples above the actual size will most probably not improve the accuracy and standard deviation of the TZ, PZ and DPU, we can expect that this might improve results for AFS regarding its accuracy and stability.

A comparison of previous and current works on segmentation of peripheral and transition zone is given in Tab. 2. Semi-automatic approaches take as additional input either a manual segmentation of the whole prostate gland ([11, 10]) or points on the prostate boundary to provide information about the shape and location of the examined prostate ([14]). The interactive work from Lijten et al. [11] achieves a DSC of 89.0 and is the best performing algorithm, followed by our proposed automatic method. For the PZ, our method performs best. Of course, while making these comparisons, one has to take into account the different datasets that were used, that varied for example in included modalities and acquisition protocols. A comparison of the AFS and DPU segmentation to other works can not be made as no previous studies on the automatic segmentation of these exist.

#### 4. CONCLUSION

This work presents a method to generate topologically correct segmentations of the TZ, PZ, DPU and AFS from axial T2w MRI. To the best of our knowledge, we are the first to address simultaneous segmentation of these four structures in an attempt to reproduce the anatomical prostate division according to the PI-RADS v2 sector map in a patient-specific manner. The presented method has the potential to improve reproducible lesion localization as well as to conduct more precise and faster therapy planning. A further contribution of our work is the ground truth data ( $n=98$ ), which will be made available for other researchers after manuscript publication.

An extensive evaluation has been undertaken to estimate inter-rater errors in manual segmentation of the zones and to compare them with the automatic results. The outcome indicated that TZ, PZ and DPU segmentations could be obtained by our method with accuracy that is in the range of inter-rater variability. On the other hand, we observed that the U-Net structure seems to be not as appropriate for the AFS as for the other structures. Thus, future work may include the exploration of other techniques such as, for example, a multi-planar approach or generative adversarial models that could make the postprocessing step redundant. Improvement of the results can be expected if more training data is used and if more experts take part in the training data generation process. Future work will additionally incorporate the transformation of the zones into a patient-specific sector map and other risk structures.

**Acknowledgements** This work has been funded by the EU and the federal state of Saxony-Anhalt, Germany under grant number FuE 74/16 and ZS/2016/04/78123 as part of the initiative 'Sachsen-Anhalt WISSENSCHAFT Schwerpunkte'. The authors would like to thank the NVIDIA Corporation for donating the Titan Xp used for this research. Data used in this research were obtained from The Cancer Imaging Archive (TCIA) sponsored by the SPIE, NCI/NIH, AAPM, and Radboud University.

#### 5. REFERENCES

- [1] J. C. Weinreb, J. O. Barentsz, P. L. Choyke, F. Cornud, M. A. Haider, K. J. Macura, D. Margolis, M. D. Schnall, F. Shtern, C. M. Tempany, H. C. Thoeny, and S. Verma, "PI-RADS Prostate Imaging - Reporting and Data System: 2015, Version 2," *Eur. Urol.*, vol. 69, no. 1, pp. 16–40, Jan 2016.
- [2] J. E. McNeal, "The zonal anatomy of the prostate," *Prostate*, vol. 2, no. 1, pp. 35–49, 1981.

**Table 2.** Quantitative comparison to previous works on segmentation of PZ and TZ. Mean distances (MAD) in *mm*.

		TZ		PZ	
Work	Input	DSC	MAD	DSC	MAD
<b>Semi-Autom.</b>					
Makni [10]	mpMRI	87.0 ± 4.0	-	76.0 ± 6.0	-
Lijtens [11]	mpMRI	<b>89.0 ± 3.0</b>	-	75.0 ± 7.0	-
Qiu [14]	T2w	82.2 ± 3.0	4.1 ± 1.1	69.1 ± 6.9	3.9 ± 1.2
<b>Automatic</b>					
Clark [12]	mpMRI	84.7 ± ?	-	-	-
Toth [13]	T2w	79.0 ± ?	1.4 ± ?	68.0 ± ?	1.0 ± ?
Chilali [15]	T2w	70.2 ± 12.1	4.5 ± 1.8	62.0 ± 7.3	5.2 ± 2.7
Mooij [16]	T2w	85.0 ± ?	-	60.0 ± ?	-
Ours	T2w	87.6 ± 6.6	<b>0.93 ± 0.32</b>	<b>79.8 ± 5.1</b>	<b>0.84 ± 0.50</b>

- [3] M. D. Greer, J. H. Shih, T. Barrett, S. Bednarova, I. Kabakus, Y. M. Law, H. Shebel, M. J. Merino, B. J. Wood, P. A. Pinto, P. L. Choyke, and B. Turkbey, "All over the map: An inter-observer agreement study of tumor location based on the PI-RADSv2 sector map," *J Magn Reson Imaging*, vol. 48, no. 2, pp. 482–490, Aug 2018.
- [4] A. Fedorov, M. G. Vangel, C. M. Tempny, and F. M. Fennessy, "Multiparametric Magnetic Resonance Imaging of the Prostate: Repeatability of Volume and Apparent Diffusion Coefficient Quantification," *Invest Radiol*, vol. 52, no. 9, pp. 538–546, 09 2017.
- [5] A. Mehrtash, A. Sedghi, M. Ghafoorian, M. Taghipour, C. M. Tempny, W. M. Wells, T. Kapur, P. Mousavi, P. Abolmaesumi, and A. Fedorov, "Classification of Clinical Significance of MRI Prostate Findings Using 3D Convolutional Neural Networks," *Proc SPIE Int Soc Opt Eng*, vol. 10134, Feb 2017.
- [6] S. Ghose, A. Oliver, R. Marti, X. Llado, J. C. Vilanova, J. Freixenet, J. Mitra, D. Sidibe, and F. Meriaudeau, "A survey of prostate segmentation methodologies in ultrasound, magnetic resonance and computed tomography images," *Comput Methods Programs Biomed*, vol. 108, no. 1, pp. 262–287, Oct 2012.
- [7] O. Ronneberger, P. Fischer, and T. Brox, "U-Net: Convolutional networks for biomedical image segmentation," *Med Image Comput Comput Assist Interv*, pp. 234–241, 2015.
- [8] Q. Zhu, B. Du, B. Turkbey, P. L. Choyke, and P. Yan, "Deeply-supervised CNN for prostate segmentation," in *2017 International Joint Conference on Neural Networks (IJCNN)*, May 2017, pp. 178–184.
- [9] A. Meyer, A. Mehrtash, M. Rak, D. Schindele, M. Schostak, C. Tempny, T. Kapur, P. Abolmaesumi, A. Fedorov, and C. Hansen, "Automatic high resolution segmentation of the prostate from multi-planar MRI," in *IEEE 15th International Symposium on Biomedical Imaging (ISBI)*, 2018, pp. 177–181.
- [10] N. Makni, A. Iancu, O. Colot, P. Puech, S. Mordon, and N. Betrouni, "Zonal segmentation of prostate using multispectral magnetic resonance images," *Medical Physics*, vol. 38, no. 11, pp. 6093–6105, 2011.
- [11] G. Litjens, O. Debats, W. van de Ven, N. Karssemeijer, and H. Huisman, "A pattern recognition approach to zonal segmentation of the prostate on MRI," *Med Image Comput Comput Assist Interv*, pp. 413–420, 2012.
- [12] T. Clark, J. Zhang, S. Baig, A. Wong, M. A. Haider, and F. Khalvati, "Fully automated segmentation of prostate whole gland and transition zone in diffusion-weighted MRI using convolutional neural networks," *J Med Imaging (Bellingham)*, vol. 4, no. 4, pp. 041307, Oct 2017.
- [13] R. Toth, J. Ribault, J. Gentile, D. Sperling, and A. Madabhushi, "Simultaneous Segmentation of Prostatic Zones Using Active Appearance Models With Multiple Coupled Levelsets," *Comput Vis Image Underst*, vol. 117, no. 9, pp. 1051–1060, Sep 2013.
- [14] W. Qiu, J. Yuan, E. Ukwatta, Y. Sun, M. Rajchl, and A. Fenster, "Dual optimization based prostate zonal segmentation in 3D MR images," *Med Image Anal*, vol. 18, no. 4, pp. 660–673, May 2014.
- [15] O. Chilali, P. Puech, S. Lakroum, M. Diaf, S. Mordon, and N. Betrouni, "Gland and Zonal Segmentation of Prostate on T2W MR Images," *J Digit Imaging*, vol. 29, no. 6, pp. 730–736, Dec 2016.
- [16] G. Mooij, I. Bagulho, and H. Huisman, "Automatic segmentation of prostate zones," *arXiv preprint arXiv:1806.07146*, 2018.
- [17] Ö. Çiçek, A. Abdulkadir, S. S. Lienkamp, T. Brox, and O. Ronneberger, "3D U-Net: learning dense volumetric segmentation from sparse annotation," *Med Image Comput Comput Assist Interv*, pp. 424–432, 2016.
- [18] G. Litjens, O. Debats, J. Barentsz, N. Karssemeijer, and H. Huisman, "Computer-aided detection of prostate cancer in MRI," *IEEE Trans Med Imaging*, vol. 33, no. 5, pp. 1083–1092, May 2014.
- [19] A. Fedorov, R. Beichel, J. Kalpathy-Cramer, J. Finet, J. C. Fillion-Robin, S. Pujol, C. Bauer, D. Jennings, F. Fennessy, M. Sonka, J. Buatti, S. Aylward, J. V. Miller, S. Pieper, and R. Kikinis, "3D Slicer as an image computing platform for the Quantitative Imaging Network," *Magn Reson Imaging*, vol. 30, no. 9, pp. 1323–1341, Nov 2012.
- [20] G. T. Herman, J. Zheng, and C. A. Bucholtz, "Shape-based interpolation," *IEEE Comput Graphics and Applications*, vol. 12, no. 3, pp. 69–79, 1992.
- [21] D. Kingma and J. Ba, "Adam: A method for stochastic optimization," *arXiv preprint arXiv:1412.6980*, 2014.
- [22] G. Litjens, R. Toth, W. van de Ven, C. Hoeks, S. Kerkstra, B. van Ginneken, G. Vincent, G. Guillard, N. Birbeck, J. Zhang, R. Strand, F. Malmberg, Y. Ou, C. Davatzikos, M. Kirschner, F. Jung, J. Yuan, W. Qiu, Q. Gao, P. E. Edwards, B. Maan, F. van der Heijden, S. Ghose, J. Mitra, J. Dowling, D. Barratt, H. Huisman, and A. Madabhushi, "Evaluation of prostate segmentation algorithms for MRI: the PROMISE12 challenge," *Med Image Anal*, vol. 18, no. 2, pp. 359–373, Feb 2014.